

RESEARCH ARTICLE

10.1002/2015JB012240

Key Points:

- A new way to look at extensional topography
- We fit coseismic, postseismic, and long-term observations with one model
- We predict that most uplift occurs within a few years after an earthquake

Correspondence to:

T. Parsons,
tparsons@usgs.gov

Citation:

Thompson, G. A., and T. Parsons (2016), Vertical deformation associated with normal fault systems evolved over coseismic, postseismic, and multiseismic periods, *J. Geophys. Res. Solid Earth*, 121, doi:10.1002/2015JB012240.

Received 26 MAY 2015

Accepted 24 FEB 2016

Accepted article online 1 MAR 2016

Vertical deformation associated with normal fault systems evolved over coseismic, postseismic, and multiseismic periods

George A. Thompson¹ and Tom Parsons²
¹Department of Geophysics, Stanford University, Stanford, California, USA, ²U.S. Geological Survey, Menlo Park, California, USA

Abstract Vertical deformation of extensional provinces varies significantly and in seemingly contradictory ways. Sparse but robust geodetic, seismic, and geologic observations in the Basin and Range province of the western United States indicate that immediately after an earthquake, vertical change primarily occurs as subsidence of the normal fault hanging wall. A few decades later, a ± 100 km wide zone is symmetrically uplifted. The preserved topography of long-term rifting shows bent and tilted footwall flanks rising high above deep basins. We develop finite element models subjected to extensional and gravitational forces to study time-varying deformation associated with normal faulting. We replicate observations with a model that has a weak upper mantle overlain by a stronger lower crust and a breakable elastic upper crust. A 60° dipping normal fault cuts through the upper crust and extends through the lower crust to simulate an underlying shear zone. Stretching the model under gravity demonstrates that asymmetric slip via collapse of the hanging wall is a natural consequence of coseismic deformation. Focused flow in the upper mantle imposed by deformation of the lower crust localizes uplift under the footwall; the breakable upper crust is a necessary model feature to replicate footwall bending over the observed width (< 10 km), which is predicted to take place within 1–2 decades after each large earthquake. Thus the best-preserved topographic signature of rifting is expected to occur early in the postseismic period. The relatively stronger lower crust in our models is necessary to replicate broader postseismic uplift that is observed geodetically in subsequent decades.

1. Introduction

It is common to neglect gravity and assume that fault-block mountains like those of the Basin and Range province of the western United States or the rift valleys of Africa shift up or down symmetrically [e.g., Segall, 2010 (p. 283); Okada, 1992] with each incremental earthquake along the normal faults that separate mountain blocks from basin blocks. But coseismic observations are strongly at odds with this simple concept of symmetrical uplift and subsidence across the fault. Observed coseismic displacement of the 1954 Dixie Valley, Nevada, and the 1983 Borah Peak, Idaho, earthquakes is highly asymmetric: the basin drops but the mountain is comparatively stable. This coseismic displacement also requires transfer of mass horizontally away from the fault/discontinuity as the accumulated elastic extension of the upper crust is suddenly relieved by fault slip, elastic contraction, and a resulting slight increase in relative density in broad regions on both sides of the fault [e.g., Hampel and Hetzel, 2015]. The resultant gravitational unloading of the fault zone produces a postseismic isostatic arching observed half a century after the Dixie Valley earthquake that is much broader than the scale of basins and ranges. One of our modeling objectives is to examine the extent to which short-term (decadal) postseismic deformation, a period when the buoyant forces of footwall unloading are largest but for which there are no reliable observations, may produce footwall uplift.

In addition to the sparse coseismic and postseismic observations, the abundant geological record supplies a third set of reliable observations. Because the coseismic displacements in large ground breaking earthquakes are on the order of meters and the observed geologic displacements are on the order of kilometers, multiseismic displacements in the hundreds or thousands are required over geologic time to build the tilted ranges and basins of the present landscape [e.g., King et al., 1988]. We focus our study on the faulting, tilting, and folding that created the present basin-range morphology, primarily during the last 10–15 million years, although earlier deformation, including metamorphic core complexes and normal faults of a different orientation, within the ranges is common. The multiseismic uplift of ranges or subsidence of basins is relative and not easily referenced to sea level as are the geodetically measured coseismic displacements and postseismic broad arching. For example, a fault block could be tilted to form a range and a basin either by subsidence of

the basin side or uplift of the mountainside. Moreover, a growing consensus that the Basin and Range region was once high like the Altiplano of the Andes [e.g., *DeCelles*, 2004; *Dickinson*, 2006; *Cassel et al.*, 2014] and has been subsiding regionally during late Cenozoic extension to its present mean elevation of about 1.5 km suggests that the basins have been going down more than the ranges have been going up. One of our objectives is to model and assess the process in order to evaluate the relative importance of localized range uplift and basin subsidence. Not included in the modeling is amplification of the tilting by erosion of the high side and deposition on the low side, nonsteady state deformation, and/or changing thermal conditions.

Elevated rift shoulders, in general, are relevant to the process. Plateaus bordered by rifts usually have elevated margins, and it is simpler to postulate that most of this structural relief is caused by uplift of the margins rather than subsidence of the entire plateau. The Colorado Plateau, for example, has uplifted margins, such as the Wasatch Range at the boundary with the Basin and Range province. The African rifts have uplifted margins, and many of the streams drain away from the rift margins toward the interior of the plateau. A particularly good example of stream reversal on the eastern flank of the western rift in Africa is illustrated and discussed by *Holmes* [1965, p.1057–1059]. It was also in Africa where *Vening Meinesz* [1950] first analyzed the isostatic forces produced by footwall unloading in a strong crust accompanying normal faulting and thus supplied a clear mechanism for footwall uplift producing the elevated rift shoulders. Footwall bending and uplift also characterizes the northwestern boundary of the Basin and Range province, where the Warner Range and Surprise Valley supply unusually good stratigraphic and geophysical evidence for use in modeling.

2. Observations

Here we outline the key observations we seek to explain with numerical models. The structural effect on the topography in extensional systems differs depending on the period examined. We begin with coseismic observations taken in 1954 and 1955 just before and after the December 1954 $M=7.2$ Fairview Peak and $M=6.5$ Dixie Valley earthquakes and also identify other observational cases, though these are sparse because the recurrence intervals tend to be long. We then discuss postseismic geodetic measurements and, finally, geologic characteristics that result from repeated slip episodes.

2.1. The 1954 Earthquake Series

Four oblique slip $M \geq 6$ earthquakes occurred during the last half of 1954 in the central Nevada seismic belt (Figure 1) [*Doser*, 1986]. The first two earthquakes happened on the Rainbow Mountain fault, west of Dixie Valley: a 6 July $M=6.2$ shock and a 24 August $M=6.5$ event. About 4 months later on 16 December, the $M=7.5$ oblique slip Fairview Peak and $M=6.5$ Dixie Valley earthquakes ruptured just 4 min and 20 s apart. The Dixie Valley event was primarily a dip-slip normal faulting earthquake. These earthquakes are part of a larger chain of events that began with the 1915 $M=7.6$ Pleasant Valley earthquake to the north and the 1932 $M=7.2$ Cedar Mountain shock to the south [*Doser*, 1988].

2.2. Coseismic Observations

A fortuitous circumstance led to a tight temporally constrained set of geodetic observations associated with the 1954 earthquake series. The United States Coast and Geodetic Survey extended a triangulation survey into central Nevada during the summer of 1954, some of which was measured prior to the July–December earthquake series [*Whitten*, 1957]. The same team reoccupied the sites during the following summer of 1955. Importantly, the sites were all leveled during the follow up campaign. *Meister et al.* [1968] reported on these results as they pertained to coseismic strain, of which the vertical component is reprised in Figure 1. These observations may include some immediate postseismic deformation, but we refer to them as “coseismic” to differentiate them from longer-term geodetic observations. A key observation is that most of the vertical coseismic deformation occurred as subsidence of the hanging wall, whereas the footwall position remained almost unchanged; this was determined from profiles that crossed the Fairview and Dixie Valley faults (Figure 1) [*Whitten*, 1957; *Meister et al.*, 1968; *Koseluk and Bischke*, 1981; *Hodgkinson et al.*, 1996].

Additional examples are sparse, but consistent with the Dixie Valley case. First- and second-order measures of elevation changes were recorded after the 1983 $M=7.0$ Borah Peak normal fault earthquake in Idaho that was compared with 1933 and 1948 surveys at the same benchmarks. Differencing by *Stein and Barrientos* [1985] is shown in Figure 1. Modeling of the Borah Peak and Hebgen Lake earthquakes [*Dempsey et al.*, 2012] also demonstrates the predominance of subsidence. Geodetic observations taken shortly after the 1981 Gulf of

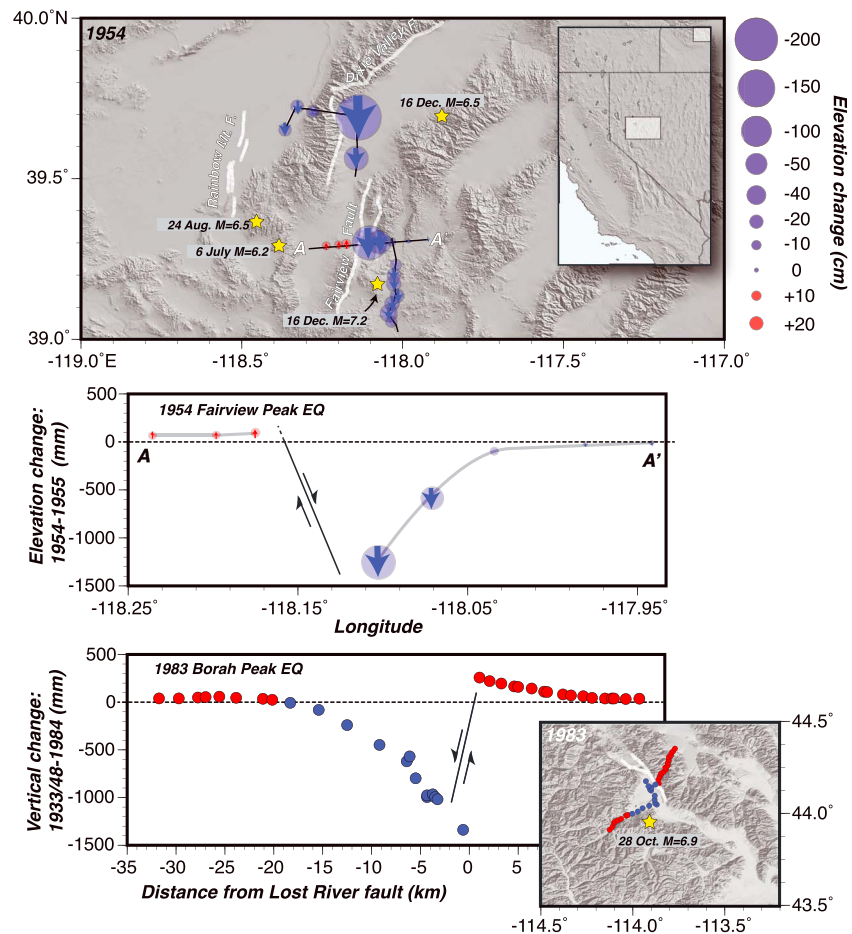


Figure 1. (top) Results [Meister *et al.*, 1968] from differencing vertical components of first-order triangulation and leveling surveys conducted during the summer of 1954 and repeated in 1955 after the December 1954 $M = 7.2$ Fairview Peak and $M = 6.5$ Dixie Valley earthquakes. The primary observations from the survey lines are subsidence of the hanging wall and a very slight uplift of the footwall. Inset map gives location. (middle) A line crossing the Fairview fault (A-A') that demonstrates that the primary coseismic effect is hanging wall subsidence compared with an almost unchanged footwall position. (bottom) A similar profile measured across the Lost River fault after the 1983 $M = 7.0$ Borah Peak earthquake [Stein and Barrientos, 1985].

Corinth earthquakes in Greece show an order of magnitude greater subsidence of the hanging wall relative to footwall uplift [Stiros *et al.*, 2007]. Thrust faulting, in contrast, is expected to produce predominantly uplift of the hanging wall, as observed by Stein *et al.* [1988] on the White Wolf fault in California; this also was well demonstrated in the Meckering earthquake in Australia, which displaced a well-surveyed pipeline [Vogfjord and Langston, 1987]. Strong coseismic slip asymmetry is demonstrated again, with most of the displacement occurring as hanging wall displacement.

These observations imply that the flank uplift in the footwalls of normal faults (the ranges of the Basin and Range province) is not a coseismic effect. Thus, slip during normal faulting is not symmetric, as standard dislocation models for fault slip are posed [e.g., Okada, 1992], but is instead asymmetric. We explore the implications of this in later sections using a finite element model in which asymmetric slip can be replicated and simulated.

2.3. Postseismic Observations

We rely on two summaries of vertical postseismic deformation in the central Nevada seismic belt; Gourmelen and Amelung [2005] isolated the vertical component of deformation as measured using interferometric synthetic aperture radar (InSAR) observations, and Hammond *et al.* [2012] developed a comprehensive database of vertical GPS and InSAR measurements (Figure 2). We reproduce the Hammond *et al.* [2012] contours of vertical velocity, draw three profiles across the Dixie Valley fault, and generate a close-up plot around the Dixie Valley region to give a general idea of the pattern of postseismic vertical change (Figure 2).

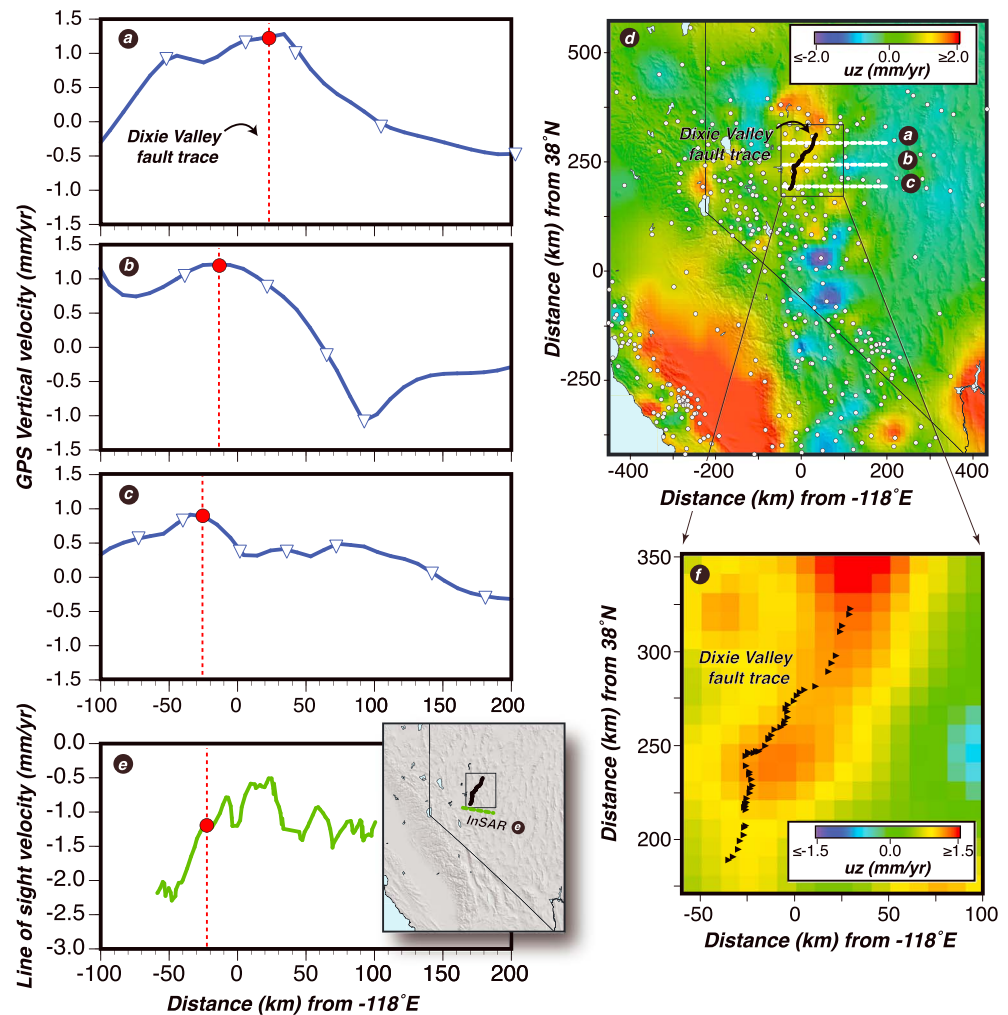


Figure 2. (a–c) Cross lines through (d) a compilation of GPS-derived vertical velocity data [Hammond *et al.*, 2012] and (e) line-of-sight change from InSAR data interpreted as primarily vertical by Gournelen and Amelung [2005]. White triangles show GPS station locations that are on or very near profiles in Figures 2a–2c, and white dots show station locations in Figure 2d. Red dashed lines give the position of the Dixie Valley fault trace in Figures 2a–2c and 2e, as do the black triangles in Figures 2d–2f. The observed pattern of postseismic elevation change is broad at ~100–200 km wide. In Figure 2f a detailed plot of elevation change from GPS near the Dixie Valley fault is shown.

Unlike the coseismic observations, the postseismic signature is one of broad uplift distributed symmetrically around the surface trace of the east dipping fault (Figure 2). The uplift rate is as high as 1.5 mm/yr averaged over the duration of measurements. Current central Nevada uplift has been modeled as postseismic relaxation in the lower crust and upper mantle that responded to stress changes induced by the 1915–1954 earthquake series [e.g., Wernicke *et al.*, 2000; Hetland and Hager, 2003; Hammond and Thatcher, 2004; Gournelen and Amelung, 2005; Hammond *et al.*, 2009]. In this paper we model a combination of postseismic crustal and/or mantle flow and gravity-driven isostatic response to study the structural relief associated with normal fault slip on a variety of time scales.

2.4. Multiseismic Observations

We use the term “multiseismic” to describe effects from repeated earthquakes that cause large cumulative fault offsets. Permanent deformation of the crust resulting from large slip (>1 km) on normal faults is evident in the morphology of the Basin and Range province, where ranges are bent and tilted away from their controlling faults (Figure 3). Range bending and tilting is identified by measured dips of initially flat lying, preextensional stratified rocks that display a postextensional range in dip from 0° to 45° [e.g., Stewart, 1998] (Figure 4).

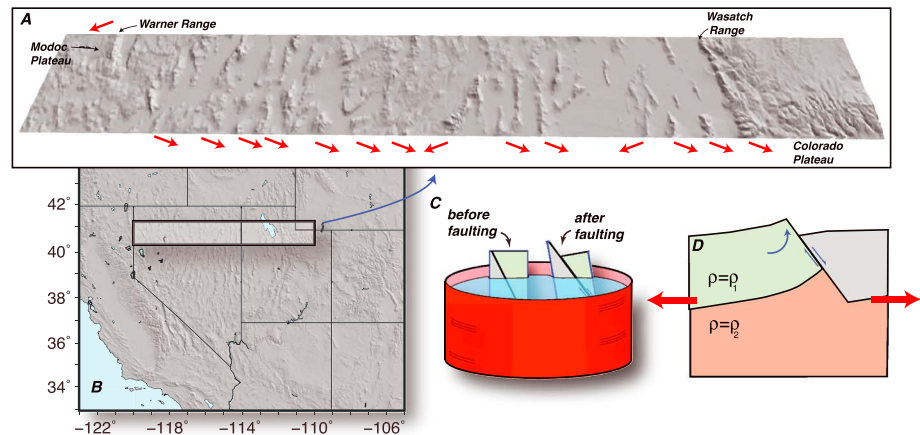


Figure 3. (a) The long-term signature of normal faulting is one of bent/tilted fault blocks and intervening basins. Red arrows show the downward inclination directions in the footwalls of Basin and Range province normal faults as determined from measured dips of preextensional stratified and volcanic rocks compiled by Stewart [1998]. A likely cause of these dips is (c) the isostatic effect of unloading of the footwalls during faulting, and (d) the resulting uplift of faulted blocks [Vening Meinesz, 1950].

Plastic bending of rift flanks is an expected effect of isostatic uplift from unloading of the footwall [e.g., Ebinger *et al.*, 1991; Hassani and Chéry, 1996; Upcott *et al.*, 1996; Thompson and Parsons, 2009] (Figure 3c). Bending is not restricted to sedimentary rocks but is observed to involve crystalline basement rocks by small slips on myriad fractures [Compton, 1966]. Accompanying flattening of normal faults and/or changes in dip with depth is another generally observed feature of large offset normal faulting [e.g., Stewart, 1978; Buck, 1988].

3. Modeling

We build a 3-D finite element model to replicate normal faulting and calculate its effects on structural topography. We define structural topography here as the relief caused directly or indirectly by slip on faults. Topographic changes caused by erosion and/or sedimentation are not simulated. The purpose of the model is to predict the topographic changes over a variety of time scales caused by fault slip, which includes isostatic

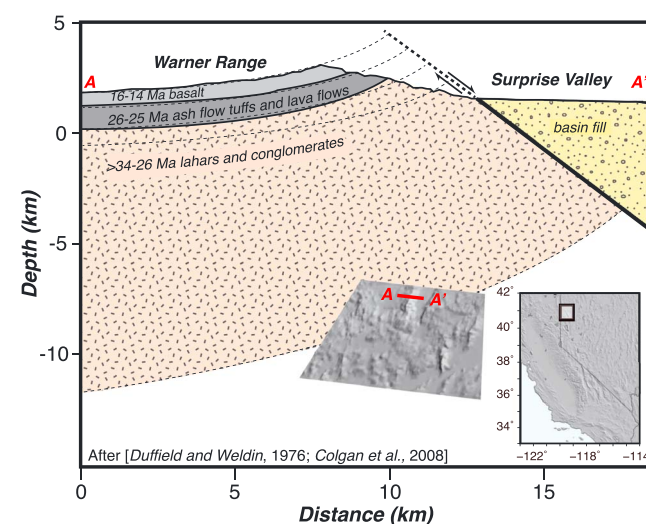


Figure 4. Cross section through the Warner Range of northwest Nevada showing tilt (15–25°) and curvature in the footwall rocks that resulted from slip on the Surprise Valley fault (adapted from Duffield and Weldin [1976] and Colgan *et al.* [2008]). Losses from erosion are approximately restored by extrapolation.

uplift, tilting, bending of both the hanging wall and the footwall, and lower crustal and upper mantle flow. This model simplifies the actual process but is more realistic than the original idea proposed by Vening Meinesz [1950]. The model has a 15 km thick elastic/plastic crust overlying a 15 km thick ductile lower crust (Parsons [1995], and references contained within) and a 170 km thick upper mantle layer (Figure 5). The upper crust relaxes stress by permanent deformation including slip on faults, and the lower layers relax stress by ductile creep. There are thus no stress discontinuities on their boundaries. We use a silicic composition for the upper crust and a more mafic layer for the lower crust based on deep seismic reflection and refraction experiments recorded in Nevada [Holbrook *et al.*, 1991]. The models are conducted with ANSYS® commercial finite element modeling software.

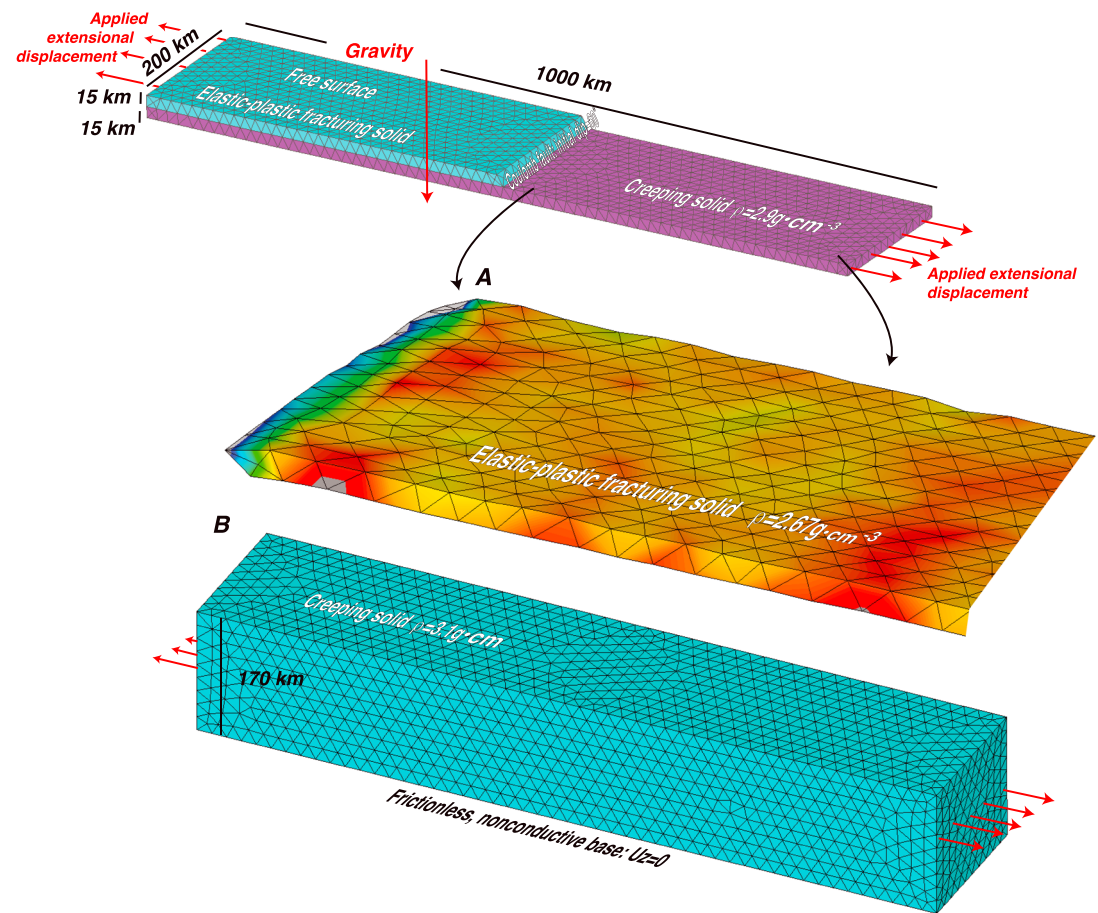


Figure 5. Three-dimensional finite element model geometry. (a) An elastic-plastic upper crust floats above (b) a ductile, creeping lower crust and upper mantle. An initially 60° dipping fault cuts through the upper crust and slips when the model's edges are displaced in extension. We use the model to investigate and quantify the role of footwall unloading and lower crustal/upper mantle accommodation on the vertical change at the surface over different time scales. An important model component in the upper crust is quasi-plastic deformation by cracking that enables it to bend and deform in more realistic fashion than an unbreakable, elastic solid, which, for example, would have a very broad bending moment. Color patterns in Figure 5a show an example of relative vertical deformation caused by localized fracturing.

The lithospheric depth where primary strain response to upper crustal faulting occurs remains unknown. The lower crust beneath the Basin and Range province is mafic in composition, with active sill intrusions accompanying extension [e.g., Christiansen and McKee, 1978; Brown, 1987; Lucchitta, 1990; Holbrook et al., 1991; Jarchow et al., 1993; Wannamaker et al., 2008; Putirka and Platt, 2012]. The lower crust is thus expected to have low viscosity because of the associated high temperatures and possible presence of fluids. A suite of numerical and geodetic models suggests that the seismogenic crust is decoupled from the mantle because lower crustal rocks are expected to be weaker than the upper mantle at similar temperature [e.g., Harry et al., 1993; Liu and Furlong, 1994; Zeyen et al., 1997; Deng et al., 1998; Liu and Shen, 1998; Brun, 1999; Liu, 2001; Wang et al., 2009]. Other models permit a weaker lower crust but do not require one [e.g., Nishimura and Thatcher, 2003; Flesch et al., 2007]. However, modeling studies of postseismic response to the 1992 $M = 7.4$ Landers and 1959 $M = 7.3$ Hebgen Lake earthquakes find the best fit with a lower crustal layer that is stronger than the upper mantle [e.g., Pollitz et al., 2000; Freed et al., 2007; Hammond et al., 2009; Chang et al., 2013]. This rheology is also found to fit the isostatic rebound from the drying of Pleistocene-aged Lake Lahontan [Bills et al., 2007] and Lake Bonneville [Bills and May, 1987].

A further constraint is introduced in the context of vertical displacement; the Moho across the Basin and Range province is smooth and unfaulted, with depth varying between 30 and 35 km across the province with little relief ($<1\text{--}2$ km) detected between adjacent basins and ranges [Klemperer et al., 1986; Brown, 1987].

Table 1. Material Constants Used in the Three Layers of the Finite Element Model^a

Parameter	0–15 km	Reference	15–30 km	Reference	>30 km	Reference
f , internal friction	0.6	1	N/A		N/A	
E , Young's modulus	$8.0 \cdot 10^4$ MPa	2	$9.0 \cdot 10^4$ MPa	2	$1.9 \cdot 10^5$ MPa	2
A , flow law	N/A		$6.3 \cdot 10^{-2} \text{MPa}^{-n_s} \text{s}^{-1}$	6	$5.0 \cdot 10^3 \text{MPa}^{-n_s} \text{s}^{-1}$	7
n , flow law	N/A		3.1	6	3.8	7
Q , activation energy	N/A		276 KJ/mol	6	492 KJ/mol	7
λ , Poisson's ratio	0.25	4	0.26	4	0.28	4
ρ , density	$2.7 \cdot 10^3 \text{kg}^3 \cdot \text{m}^{-3}$	5	$2.8 \cdot 10^3 \text{kg}^3 \cdot \text{m}^{-3}$	5	$3.1 \cdot 10^3 \text{kg}^3 \cdot \text{m}^{-3}$	5

^aElements in the upper crust are elastic crackable and fail at a threshold differential stress according to an internal friction coefficient. Elements in the lower crust and upper mantle are viscoelastic, with rate-dependent creep behavior controlled by the temperature gradient and the listed constants. References: (1) *Byerlee* [1978], (2) *Birch* [1966], (3) *Hansen and Carter* [1983], (4) *Christensen* [1996], (5) *Christensen and Mooney* [1995], (6) *Caristan* [1982], and (7) *Carter and Tsenn* [1987].

This observation suggests that if significant postseismic compensation from dip-slip faults occurs in the upper mantle, then the lower crust must equilibrate over a longer time scale. We address this uncertainty by conducting models that have weak and strong lower crustal layers, as well as a variety of upper mantle rheologies.

The elastic/plastic upper crust is modeled using 8 node (including midside nodes), breakable tetrahedral elements (Figure 5). The physical properties of the upper crust are taken from measurements on fully saturated Westerly granite and are described by four elastic constants: Young's modulus (E), density (ρ), Poisson's ratio (λ), and an internal friction coefficient (f) (Table 1). These elastic/plastic elements are engineered by ANSYS to replicate rock behavior; the elements behave elastically up to a critical stress level and then exhibit permanent deformation through cracking. This happens when the defined strength of the element [*Birch*, 1966; *Christensen*, 1996] is overcome by the calculated differential stress magnitude. Failure occurs on planes defined by the stress tensor and coefficient of internal friction for granite ($\mu = 0.6$) [*Byerlee*, 1978].

Crack formation at an element integration point is characterized by changing the stress-strain relation through definition of a plane of weakness in a direction orthogonal to the crack. Additionally, a shear strength reduction is calculated that affects subsequent loading that induces sliding on the crack plane. Multiple cracks can occur at a single integration point in response to changing stress orientations. This process is expressed by the William-Warneke failure criterion for three nontensional principal stresses as

$$\frac{F}{f_c} - S \geq 0 \quad (1)$$

[*William and Warnke*, 1975]. The parameter f_c is the material uniaxial crushing strength as derived from elastic properties, and is F is a function of the principal stresses as

$$F = \frac{1}{\sqrt{15}} \left[(\sigma_1 - \sigma_2)^2 + (\sigma_2 - \sigma_3)^2 + (\sigma_3 - \sigma_1)^2 \right]^{\frac{1}{2}}. \quad (2)$$

The term S is defined as

$$S = \frac{2r_2(r_2^2 - r_1^2)\cos \eta + r_2(2r_1 - r_2)[4(r_2^2 - r_1^2)\cos^2 \eta + 5r_1^2 - 4r_1r_2]^{\frac{1}{2}}}{4(r_2^2 - r_1^2)\cos^2 \eta + (r_2 - 2r_1)^2}, \quad (3)$$

where

$$\cos \eta = \frac{2\sigma_1 - \sigma_2 - \sigma_3}{\sqrt{2} \left[(\sigma_1 - \sigma_2)^2 + (\sigma_2 - \sigma_3)^2 + (\sigma_3 - \sigma_1)^2 \right]^{\frac{1}{2}}},$$

and η is the angle of similarity which describes relative magnitudes of the principal stresses (σ_1, σ_3). The parameters r_1 and r_2 are radii that are found as a function of material strength and stress to ensure that the failure surface is closed and are solved for in a system of equations constrained by that closure.

Element fracturing and accompanying plastic deformation enable the upper crustal layer to deform at scales that are consistent with real world observations. In contrast, a perfectly elastic solid can store essentially infinite stress and will bend/deflect at a width defined only by its length and bounding conditions [e.g., *Watts and Burov*, 2003]. We see elastic/plastic behavior as an essential aspect [e.g., *Hassani and Chéry*, 1996; *Lavier et al.*, 1999, 2000; *Huismans and Beaumont*, 2002; *Lavier and Buck*, 2002] in our modeling approach

because observed bending associated with the footwall and hanging wall, even on very large offset normal faults like the 9 km offset on the Surprise Valley fault, occurs over just a ~10 km span [e.g., Colgan *et al.*, 2008; Lerch *et al.*, 2010] (Figure 4).

The 15 km thick lower crustal layer has properties representative of basalt-diabase composition, and the 170 km thick mantle layer has properties associated with an average of wet and dry dunite samples (Table 1). In these two layers, differential stress σ_{ij} is related to elastic strain ε_{kl} through Hooke's law as

$$\sigma_{ij} = \sum_{k=1}^3 \sum_{l=1}^3 C_{ijkl} \varepsilon_{kl}, \quad (4)$$

Modeled viscoelastic strain rate ($\dot{\varepsilon}$) is controlled by the creep equation as

$$\dot{\varepsilon} = A \exp(-Q_c/RT) \sigma^n \quad (5)$$

(1-D form for simplicity) [e.g., Kirby and Kronenberg, 1987], where A , Q_c , and n are experimentally derived constants (Table 1) [Birch, 1966; Caristan, 1982; Christensen and Mooney, 1995; Christensen, 1996], R is the universal gas constant, and T is temperature. Calculations in ANSYS are conducted as a matrix form of equation (5), we do not give all the solution components here for space considerations. There is not an explicit time variable in equations (4) and (5); however, the differential stress is a function of time in our models, especially after earthquake slip is imposed.

To extrapolate surface temperature to depth, we use the relation

$$T(z) = T_0 + \left(\frac{q^*}{K}\right)z + \left(\frac{\gamma_0 H^2}{K}\right) \left[1 - \exp\left(\frac{-z}{H}\right)\right], \quad (6)$$

[Meissner, 1986] where z is depth, T is temperature (T_0 is the temperature at the surface), K is the thermal conductivity, γ_0 is the heat production value, which is calculated using an exponential decay law as $\gamma = \gamma_0/e$ ($z = H$) [Lachenbruch, 1968], where H is the relaxation depth (base of the upper crust), and $q^* = q^0 + AH$, where q^0 is surface heat flow (averages 79 mW m⁻² based on four local wells) [Blackwell and Richards, 2004]. For reference and comparison with other published estimates, dynamic viscosity can be calculated from

$$\mu = \sigma^{1-n} \exp(Q_c/RT) / 2A, \quad (7)$$

where σ is differential stress as calculated by the finite element model.

We model slipping normal faults as initially constant, 60° east dipping cuts through the upper crust. We produce models with a single east dipping normal fault and models with two faults at a variety of spacing. The faults are deformable because they are made from zero thickness contact elements that are welded to the underlying offset crustal blocks. Contact elements function under Coulomb failure theory, which slip when $CF \equiv \bar{\tau}_f + f\sigma_n$ exceeds zero. Variable $\bar{\tau}_f$ is shear stress resolved on the contact plane, f is the coefficient of friction, and σ_n is normal stress. The role of pore fluids is neglected. The friction coefficient is arbitrarily set to $f = 0.2$ as we are interested in relative behaviors. There is a linear relation between the shear stress state and friction; however, we either keep faults locked, allow them to slip at steady state to replicate multiseismic slip, or induce instantaneous seismic slip of prescribed amounts by moving the two-fault walls by a defined offset. Thus, the friction coefficient is not influential. The faults exist in the upper and lower crust but can be locked and prevented from slipping depending on modeling choices.

The top of the model is unconstrained (free surface) and starts out with no relief. The northern and southern boundaries cannot move in the north-south directions but are allowed to deform in all other directions. The model base can move horizontally but not vertically. The base is sufficiently deep (200 km) to avoid affecting the shallower parts of the model, and it is kept in thermal equilibrium. No other limits are prescribed other than gravitational loading and defined earthquake slip for some applications.

The model is initiated by stretching it symmetrically over incremental displacement of the western and eastern edges until it is extended by 10%. Extension of the upper crust occurs mostly through displacement of the normal fault(s), though a small fraction happens through plastic strain (cracking). For the initial period we do not simulate individual earthquakes but instead allow the fault(s) in the models to slip (creep) continuously. The idea is to condition the stress in the crust and mantle to approximate that of a long-lived extensional system like the Basin and Range province.

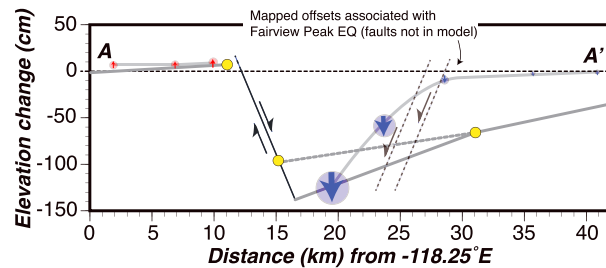


Figure 6. Model results showing coseismic contributions to extensional topography, which is almost completely restricted to hanging wall subsidence. The modeled elevation change (yellow dots) does not match the observed in the hanging wall because, while it does have internal fracturing that enables bending, it lacks the more continuous, subsidiary faults that broke in the hanging wall during the Dixie Valley and Fairview Peak earthquakes [e.g., Caskey *et al.*, 1996]. The modeled earthquake has 1 m of coseismic slip, whereas the Dixie Valley earthquake had unusually large (1.4 m) coseismic subsidence measured at the surface for a $M = 6.5$ earthquake.

the sharp (5 km wide) downward deflection of the hanging wall, which we suspect may be in part due to sympathetic slip on subsidiary faults in the hanging wall that were offset after the Dixie Valley and Fairview Peak earthquakes [e.g., Caskey *et al.*, 1996]. We think that the most important result here is that there appears to be a physical basis (gravity) for asymmetric coseismic slip on normal faults, with slip comprised entirely of hanging wall subsidence. Additionally, this initially asymmetric slip in the upper crust has implications on the underlying lithosphere.

Coseismic deformation affects the lithosphere beneath the seismogenic crust in two ways: (1) extension of the crust pulls the hanging wall away from the footwall, and (2) the hanging wall collapses downward (Figure 7). The mass that is pulled away from the fault zone is transferred to the surrounding region as a slight compressional increase in density accompanying strain release. The unweighting stress on the footwall from a 1 m slip event (in 2-D) is estimated to be 70.1 MPa distributed over a line orthogonal to and beneath the fault (~8.7 km long for a 60° dipping fault that crosses the 15 km thick upper crust). Additionally, slip on the upper crustal fault imposes a static Coulomb stress increase on a theoretical extension of the normal fault into the lower crust of 0.06 MPa if a friction coefficient of $\mu = 0.2$ is assumed (Figure 7). These stress values represent effects from a single earthquake. We explore the results of these applied forces by modeling postseismic deformation in the next section.

4.2. Postseismic Deformation

Many authors have already created models that replicate the geodetic postseismic signal from central Nevada earthquakes [e.g., Wernicke *et al.*, 2000; Hetland and Hager, 2003; Hammond and Thatcher, 2004; Gourmelen and Amelung, 2005; Hammond *et al.*, 2009]. However, for our model to have validity in explaining short-term coseismic and long-term multiseismic observations, we feel it must also at least be consistent with intermediate-term postseismic data. Further, since we use a 3-D finite element approach with an elastoplastic upper crust, we are curious how well this type of model can fit postseismic observations and whether it can provide additional insights. We focus on the 1954 $M = 6.5$ Dixie Valley earthquake for postseismic study because it was a pure normal fault earthquake, whereas the Fairview Peak earthquake was oblique with about equal amounts of dextral and normal slip [e.g., Caskey *et al.*, 1996]. The Dixie Valley quake is associated with a more obvious vertical geodetic signal as well (Figure 2).

We note an apparent consensus toward the “Crème Brûlée” model of the Earth [e.g., Bürgmann and Dresen, 2008], which has a stronger lower crust than upper mantle. This type of model yields a better fit to postseismic deformation in the Basin and Range province [e.g., Pollitz *et al.*, 2000; Wernicke *et al.*, 2000; Hetland and Hager, 2003; Hammond and Thatcher, 2004; Gourmelen and Amelung, 2005; Freed *et al.*, 2007; Hammond *et al.*, 2009; Chang *et al.*, 2013]. We therefore anticipate a better fit with a strong lower crust, but we do test cases with a weak lower crust and find that they cannot reproduce the breadth of postseismic uplift (Figure 8a).

4. Model Results

4.1. Coseismic Deformation

We model coseismic elevation change by subjecting the east and west model edges to symmetrical extensional displacements, the entire model to gravity, and allowing the normal fault to slip freely. We note that the initial (coseismic) displacement in the model is entirely hanging wall subsidence, and no footwall change. This is consistent with observations made by Whitten [1957] as interpreted by Meister *et al.* [1968] (Figure 6). We find this model result in the short term before isostatic and postseismic effects can manifest as footwall uplift and broader flexure. We are not able to match observations perfectly, particularly

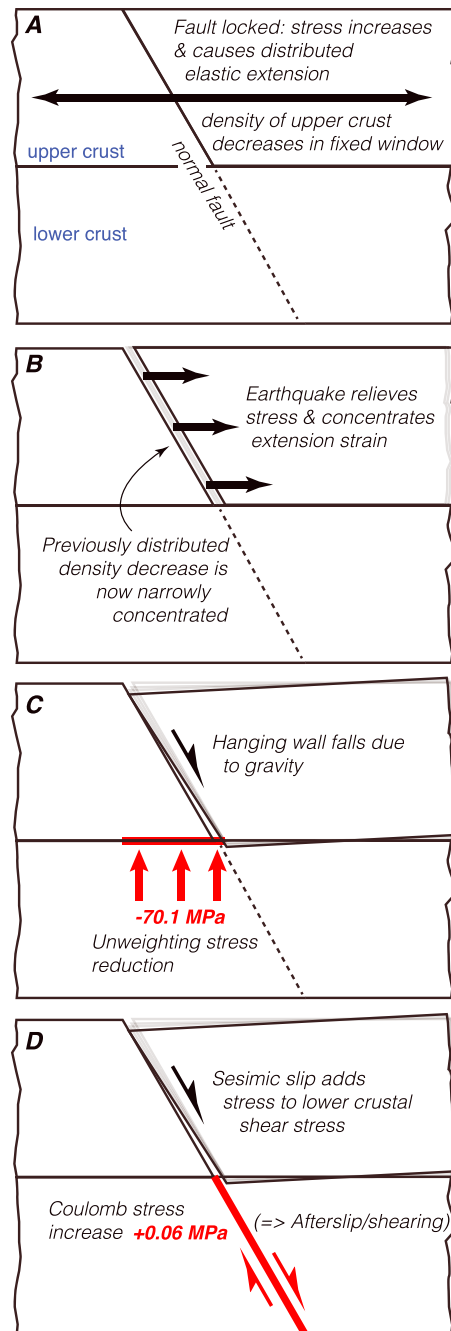


Figure 7. Diagram illustrating the imposed forces on the substrate from a slip event in the upper crust. (a) Horizontal extensional strain occurs by elastic stretching and thinning. The result is distributed loss of mass within the window shown because of remotely imposed stretching. (b) Horizontal extensional stress is relieved during an earthquake when the hanging wall is pulled away from the footwall. This focuses the loss of mass within the vicinity of faulting and unweights the footwall. The mass reduction in 2-D amounts to a 70.1 MPa upward directed stress distributed beneath the fault. (c) The hanging wall immediately collapses and subsides (e.g., Figures 1 and 6). (d) Slip on the normal fault plane induces a 0.06 MPa stress increase on a theoretical extension of the fault in the lower crust. In reality, this might be a zone of induced distributed shear and/or flow.

Our model does not spontaneously produce large stick-slip earthquake events. We therefore simulate the $M=6.5$ Dixie Valley earthquake by enforcing 1 m of hanging wall subsidence as asymmetric slip on the upper crustal fault, which is a compromise between the predicted 0.44 m of slip based on the regressions of Wells and Coppersmith [1994] and the ~ 1.4 m of observed coseismic slip at the surface (Figure 1). We then compare vertical deformation rate (mm/yr) at $t=60$ years postearthquake at nearest model nodes to locations of GPS measurements (Figure 8) for a variety of upper mantle viscosities that range from $\mu = 10^{16}$ Pa \cdot s to $\mu = 10^{20}$ Pa \cdot s. Locations are approximate because our modeled fault is perfectly straight, whereas the Dixie Valley fault is curved (Figure 8). We cannot recover reliable results at every model node because some of the elements have fractures with offsets that produce localized surface deformation. We run models with a locked lower crustal fault and others with the fault allowed to replicate afterslip/shearing.

We find that models with a strong lower crust ($\mu = 10^{25}$) and weaker upper mantle (viscosities between $\mu = 10^{18}$ Pa \cdot s and $\mu = 10^{19}$ Pa \cdot s) fit the range of GPS observations best (Figures 8c and 8d), which is in broad agreement with other studies [e.g., Pollitz et al., 2000; Wernicke et al., 2000; Hetland and Hager, 2003; Hammond and Thatcher, 2004; Gourmelen and Amelung, 2005; Freed et al., 2007; Hammond et al., 2009; Chang et al., 2013]. We do, however, require that the lower crustal fault be able to slip after the earthquake; otherwise, there is not enough displacement from the base of the lower crustal layer into the mantle to initiate flow there. Our model has node spacing on the order of 1–5 km depending on the local geometry, meaning that after-slip could either represent slip on a discrete plane or a shear zone that could be a few kilometers wide.

Surface postseismic deformation in our models is a response to mantle flow induced by the coseismic unweighting of the footwall and lower crustal shear. This causes a rapid isostatic response that is focused mostly under the footwall of the fault (Figure 9a). By 60 years after the earthquake, the model

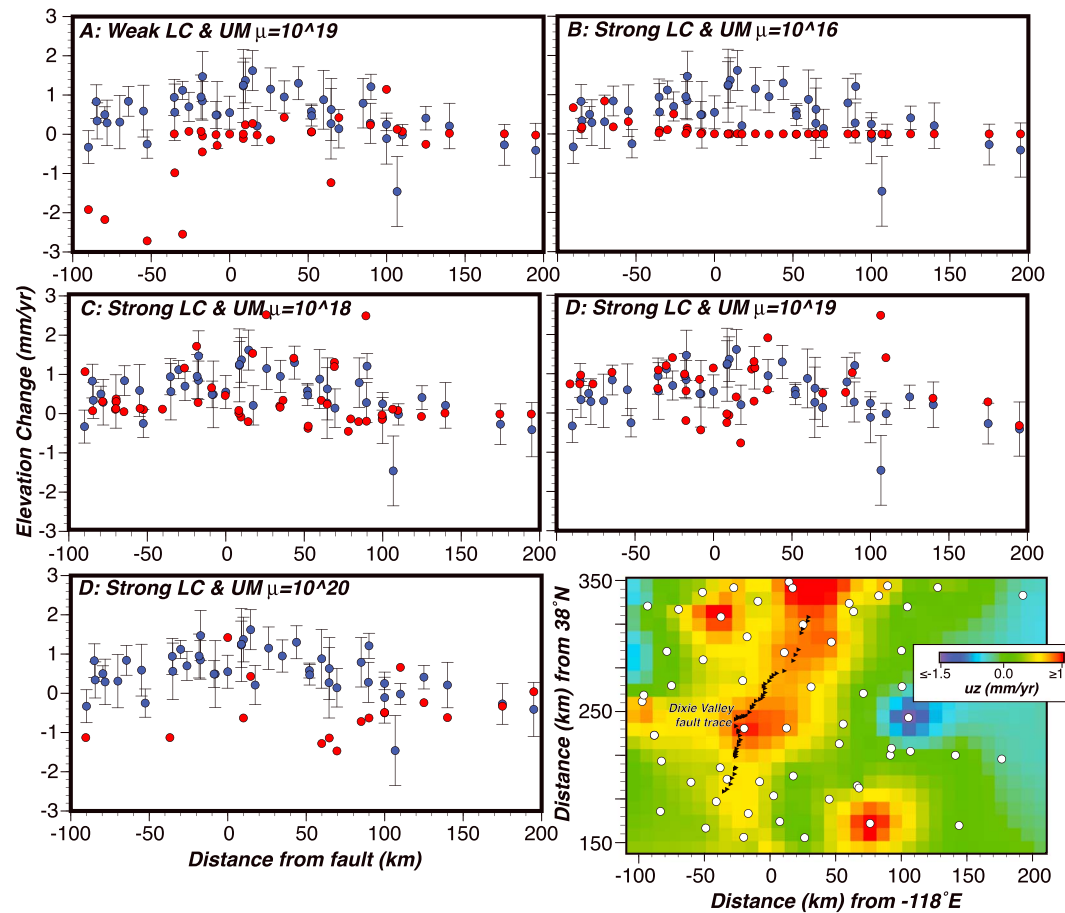


Figure 8. Model results (red dots) showing calculated surface uplift rates for a range of crustal and mantle viscosities. Results are found at nearest model nodes (within 5 km) to GPS locations (blue dots). The map at lower right reprises contoured elevation change rates from Figure 2, and the white dots give GPS observation locations from Hammond *et al.* [2012]. (a) The lower crust is as weak as the upper mantle ($\mu = 10^{19}$ Pa · s), whereas (b–d) the lower crust is strong ($\mu = 10^{25}$ Pa · s) and only the upper mantle is weak, ranging from $\mu = 10^{16}$ Pa · s to $\mu = 10^{20}$ Pa · s. We note best fits for upper mantle viscosities between $\mu = 10^{18}$ Pa · s and $\mu = 10^{19}$ Pa · s.

shows some subsidence under the hanging wall along with a migration of uplift to the west of the fault (Figure 9c). The strong lower crust causes the surface manifestation to be broad uplift on both sides of the fault with slightly more uplift on the west side (Figures 2, 8, and 9b).

Postseismic response is transient deformation that diminishes with time. We therefore calculate crustal and mantle deformation rates at additional time steps of 100 years and 150 years postearthquake to see model predictions on its future evolution. At 100 years postearthquake, deformation is lower magnitude than at 60 years (Figure 9c) and almost entirely directed upward but concentrated to the west beneath the footwall (Figure 10a). After 150 years, the model predicts transient deformation to be essentially completed (Figure 10b).

While the present-day geodetic signal has a broad, relatively consistent uplift of both the footwall and hanging wall (e.g., Figures 2 and 8), the morphology of a range front shows uplift, tilting, and bending of the footwall (Figures 3a and 4). We are curious when this preserved deformation occurs and look to the model for potential answers. Tracking the time history of deformation in the model demonstrates that rapid uplift focused under the footwall happens shortly after the simulated earthquake, particularly during the first 10 years (Figures 10a and 11). This is an expected model result because strain rate ($\dot{\epsilon}$) depends exponentially on differential stress (σ) per equation (2). Thus, the period just after the strong stress change (Figure 7) from slip on the fault would lead to high mantle strain rates. The 10 year period is also the duration of a typical Omori law aftershock decay [e.g., Parsons, 2002] that also takes an exponential form. Tiny aftershocks as small as $M - 6$ have been created in

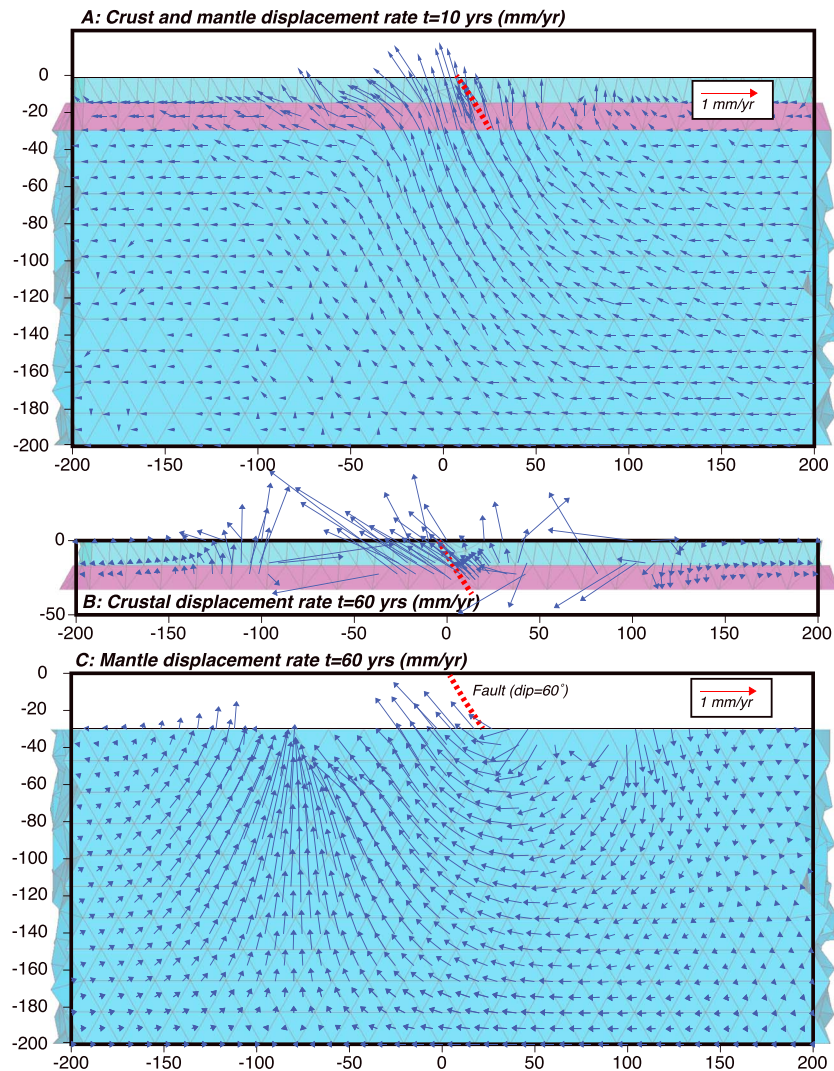


Figure 9. (a) Expected lower crustal and mantle displacement rate vectors (mm/yr) for a time 10 years after a normal fault earthquake (displacement = 1 m) shown in cross section. (b) Crustal vectors are shown at time 60 years after the earthquake, which correspond to present-day geodetic observations in the central Basin and Range (Figure 8). (c) The upper mantle deformation rate vectors are shown at time 60 years after the earthquake. These calculations are made in a model with a strong lower crust and mantle viscosity of $\mu = 10^{19}$.

laboratory experiments [McClaskey *et al.*, 2014], meaning that the plastic bending of crystalline footwall rocks might take place as small shear-fracture aftershocks shortly after the primary faulting event.

We cannot confirm rapid footwall uplift with geodetic measurements for the Dixie Valley earthquake because no short-term GPS or InSAR measures are available. The uplift rates we calculate are also dependent on the state of stress in the crust and mantle just prior to the earthquake (which are unknown in the real Earth), so we give more credence to the relative elevation rate change curves versus time than to their absolute magnitudes.

4.3. Multiseismic Deformation

Primary long-term observations associated with rift zones include uplift, tilting, and bending of the footwall [e.g., Vening Meinesz, 1950; Heiskanen and Vening Meinesz, 1958; Stewart, 1978; Ebinger *et al.*, 1991; Upcott *et al.*, 1996]. Observed short wavelength (~ 10 km) [e.g., Duffield and Weldin, 1976; Colgan *et al.*, 2008] anelastic [Compton, 1966] bending requires use of an elastic/plastic representation of the upper crust in our models. We find excellent agreement with an observed width of bending (9.1 km versus ~ 10 km) at the Warner

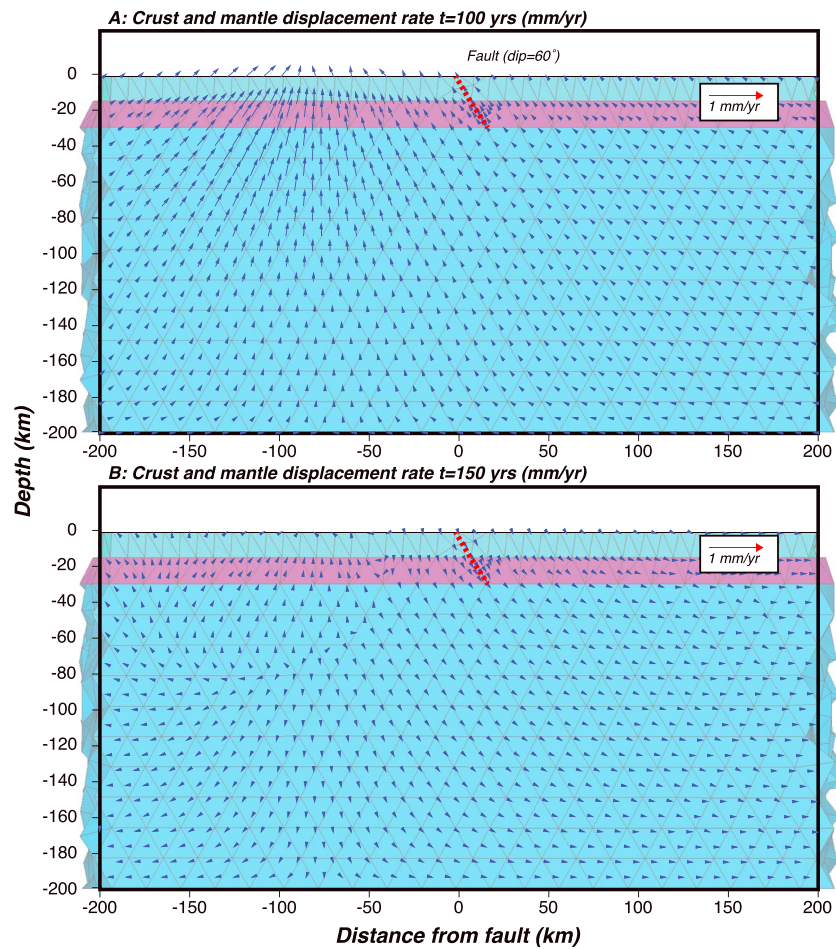


Figure 10. Expected crustal and mantle displacement rate vectors (mm/yr) at (a) 100 years after a normal fault earthquake (displacement = 1 m) and (b) after 150 years. Initial deformation is concentrated near the fault in the footwall and then shifts west. Most postseismic deformation has ceased after 150 years.

Range as constrained by Colgan *et al.* [2008] (Figure 12) if we use default physical properties for granite in our models (Table 1). In the example shown in Figure 12, the fault slipped a cumulative 4 km and produced a 1.5 km net uplift of the footwall. We do not find variation in the bending width as a function of fault offset, because this width is primarily controlled by the rheology of the underlying layers as they respond to isostasy, and the fault dip controls the width of the unweighted zone.

While the bending width is not found to be a function of fault offset, the degree of tilting/bending of the footwall is. We systematically add extensional displacements to the model edges, which have the effect of gradually increasing cumulative normal fault slip. The model then produces a roughly linear relationship between fault displacement and average inclination of the footwall (Figure 13). We compare our calculations with observations of footwall inclination compiled by Stewart [1978] and independent uplift and fault slip determinations (mostly from thermochronology) for a variety of normal faults in the Basin and Range province including the Teton fault [Byrd *et al.*, 1994], the Panamint fault [Bryant, 2000], the Wasatch Front [Ehlers *et al.*, 2003], the White Mountains [Stockli *et al.*, 2003], the Cortez Mountains (Crescent fault) [Friedrich *et al.*, 2004], the Jackson Range, the Santa Rosa Range, the Pueblo Mountains [Colgan *et al.*, 2006], and the Warner Range [Egger and Miller, 2011]. We plot the inclination and offset observations against each other in Figure 13, and while it is not certain if they represent a linear relationship, they are consistent with the range of calculated values, with a clear dependency between degree of inclination and fault offset.

We consider two possible causes of footwall inclination, bending and block rotation. We model this behavior with a pair of normal faults to test the idea that the footwall block may rotate. However, we find that there is

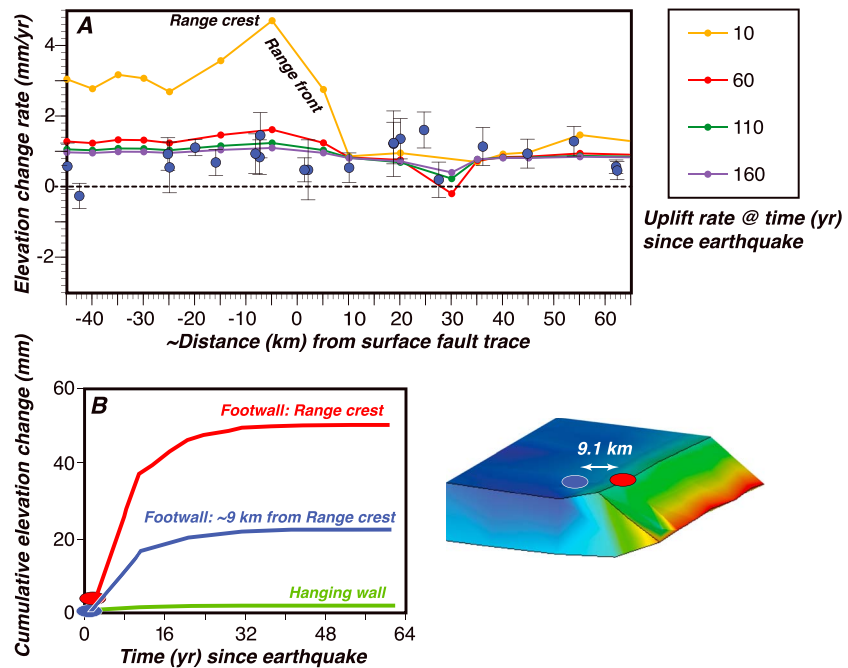


Figure 11. (a) The calculated elevation change rate at different times after a simulated earthquake (displacement = 1 m). Present-day GPS observations are shown as blue dots with error bars. Uplift is calculated to be concentrated beneath the footwall at shorter times after the earthquake (see also Figure 9a). (b) The calculated short-term deformation, which predicts high uplift rates during the first ~10 years after the earthquake. By 60 years after the earthquake, calculated rates are close to observed GPS rates. We think this fast uplift, if it occurs in the real Earth, is primarily responsible for footwall bending/tilting.

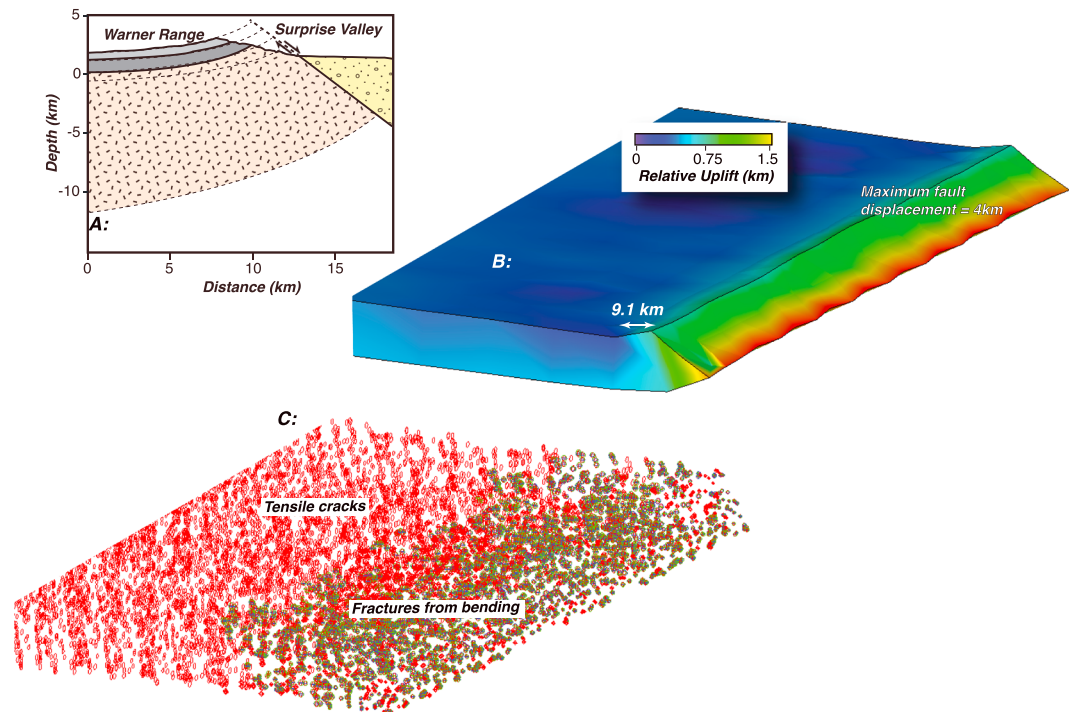


Figure 12. (a) Observed and (b) modeled footwall bending resulting from isostatic response to unloading. The Warner Range example in Figure 12a shows that most of the bending occurs in a narrow zone about 10 km wide, which is replicated closely by the model with a 9.1 km wide bending region. This is possible to replicate in the model because the upper crust is composed of crackable elements that show (c) tensile cracks distributed throughout the volume that result from extensional stress, and more intense fracture density adjacent to the fault that enables sharp bending.

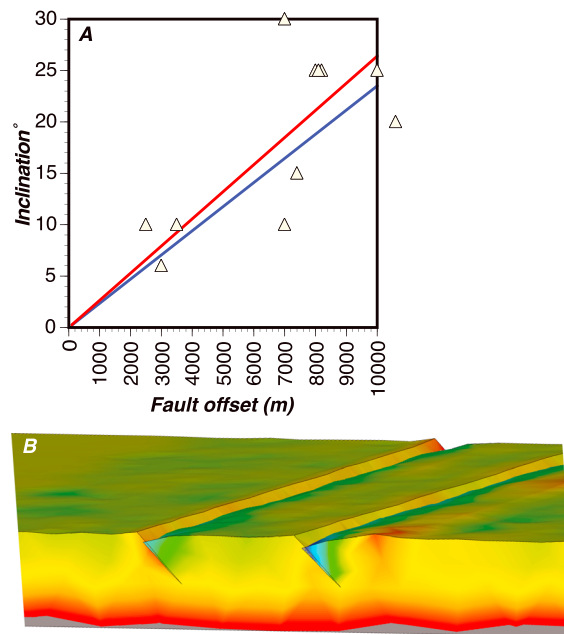


Figure 13. (a) Model results (red line) showing expected footwall inclination (dip of stratification) as a function of offset for (b) a pair of slipping normal faults spaced 40 km apart. The blue line shows results for a single-fault model for reference. Triangles in Figure 13a show observed tilting as compiled by Stewart [1978] plotted against independent uplift and fault slip determinations (mostly from thermochronology) for the Teton fault [Byrd *et al.*, 1994], the Panamint fault [Bryant, 2000], the Wasatch Front [Ehlers *et al.*, 2003], the White Mountains [Stockli *et al.*, 2003], the Cortez Mountains (Crescent fault) [Friedrich *et al.*, 2004], the Jackson Range [Colgan *et al.*, 2006], the Santa Rosa Range [Colgan *et al.*, 2006], the Pueblo Mountains [Colgan *et al.*, 2006], and the Warner Range [Egger and Miller, 2011]. We note a reasonable agreement between modeled and observed isostatic bending/tilting as a function of fault offset.

virtually no difference between calculations with a single fault versus two faults (compare the red and blue lines in Figure 13, which represent the two-fault (40 km spacing) and single-fault models, respectively). However, more closely spaced faults (<3 km) than we can model effectively are observed to rotate on progressively flattening planes that are in turn cut by new steeper faults [e.g., Proffett, 1977]. Additionally, it appears from geologic mapping in the Basin and Range province [Stewart, 1998; Stewart *et al.*, 2003] that narrower range blocks (<10–15 km) tend to have more uniform inclination than do wider blocks, which exhibit bending. These observations are consistent with our modeled ~10 km width of footwall bending because blocks of this width or less are too narrow to bend.

We note a confirmatory observational case from northwest Nevada, where two ranges lie about 25 km apart; the Nightingale on the west is bounded by a west dipping normal fault, and the Sahwave Range to the east is bounded by an east dipping normal fault (Figure 14). Detailed mapping by Van Buer [2012] shows that the two ranges are actually a single, mostly unfaulted crystalline block that has been bent into

a syncline (Figure 14). There is about 2–3 km of upwarp across the syncline, depending on the amount of erosion that has taken place. Thus, in this case, all footwall inclination resulted from bending (again at ~10 km width), with effectively zero block rotation.

Another observed consequence of isostatic deformation of the footwall in normal fault systems is a decrease in the fault dip [e.g., Stewart, 1978]. In Figure 15, we plot the calculated flattening of a normal fault as a function of offset. This relationship is slightly nonlinear in the models, whereas the average inclination change is linear (Figure 13). This is because most of the deformation occurs within 10 km of the fault plane and diminishes significantly with distance, and the average inclination is less sensitive to offset than is fault plane deformation. The model suggests that faults could have relatively low angles (~35°–40°) with very large (~10 km) offsets and agrees with observations at the Warner Range where an initially 55°–60° dipping fault now has a ~35° dip after ~8 km of offset [Lerch *et al.*, 2010; Egger and Miller, 2011].

A consequence of trying to fit observations across all time scales in our models is that we encounter trade-offs that require some compromises. For example, to match footwall bending, we must allow the upper crust to fracture. This in turn makes fitting postseismic geodetic observations at every point more difficult because the precise fracturing locations are somewhat random. Similarly, the requirement that the lower crust must be stronger than the upper mantle to fit postseismic observations means that our long-term models develop some Moho topography (Figure 16). The models do not allow for enough lower crustal flow beneath the ranges to completely equalize footwall uplift over the modeled duration. Generally, it does appear that a stronger lower crust is necessary in long-term models to fit the isostatic rebound from the drying of Pleistocene-aged Lake Lahontan ($\mu = 10^{20}$ Pa · s [Bills *et al.*, 2007]) and Lake Bonneville

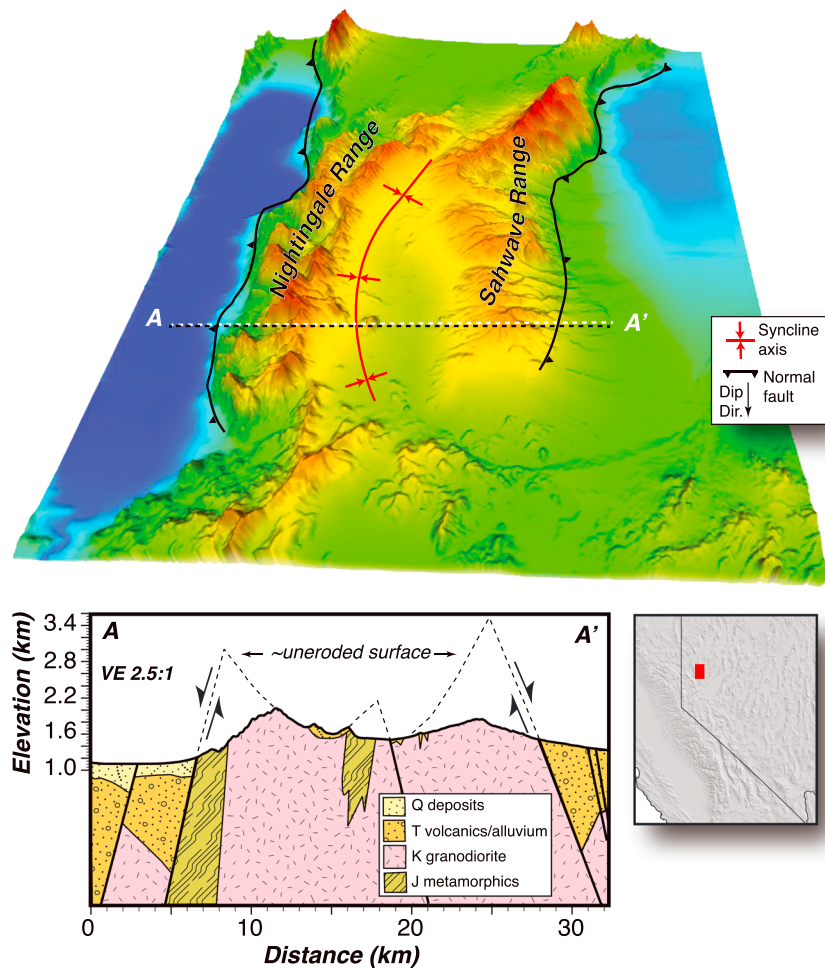


Figure 14. Topography of the Sahwave and Nightingale ranges in northwest Nevada. The two ranges are actually a single bent, synclinal crystalline block bound by east dipping and west dipping normal faults [Van Buer, 2012]. A topographic profile is shown below (vertically exaggerated by a factor of 2.5) that illustrates the synclinal shape of the footwall block. Geology and extrapolation of the uneroded surface are taken from Van Buer [2012].

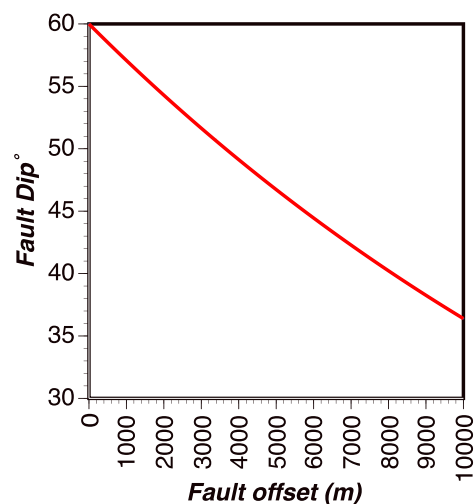


Figure 15. (a) Model results showing calculated evolution of normal fault dip as a function of offset. The initial dip is set to 60° but can evolve to low angles after significant offsets in the model.

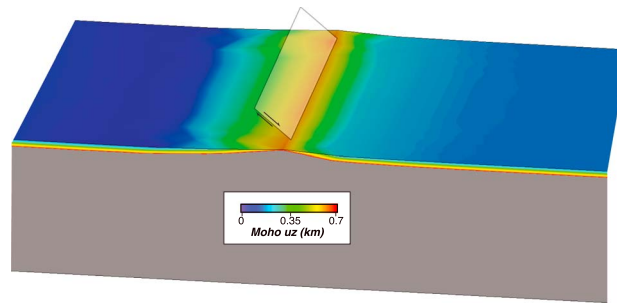


Figure 16. A consequence of long-term slip on a normal fault system with a relatively strong lower crustal layer is that the Moho boundary is subject to deformation. A strong lower crust is necessary to model postseismic deformation (Figure 6). In this example the normal fault has ~4 km of offset that leads to ~0.7 km of relief on the Moho, which is below the resolution of seismic observations [e.g., Klempner et al., 1986; Brown, 1987]. There may be time-dependent lower crustal rheology that allows long-term flattening of the Moho, and/or it is magmatically intruded.

($\mu = 10^{22}$ Pa · s [Karow and Hampel, 2010; Bills and May, 1987]). These values are lower than the strong and/or fully elastic lower crustal layers employed for postseismic modeling of vertical deformation [e.g., Nishimura and Thatcher, 2003; Gournelen and Amelung, 2005] as well as the $\mu = 10^{25}$ Pa · s value we used. Therefore, it is possible that a time-dependent rheology might be in effect such that over the very long time frame (10^5 – 10^6) years the lower crust is less viscous than it is in the postseismic period (10^1 – 10^2 years). For example, localized magmatic intrusions could cause this effect.

Given that a creep rheology can be stress dependent (equation (5)), it might be expected to vary over single and/or multiple seismic cycles, since slip on a fault can alter the surrounding stress field [e.g., Yamashina, 1978; Das and Scholz, 1981; Stein and Lisowski, 1983]. We note in our long-term models that a region extending about 50–60 km on either side of our modeled normal fault has increased horizontal least stress resulting from slip on the fault (Figure 17). A differential stress decrease like this would have the effect of increasing mantle/lower crustal viscosity and inhibiting crustal normal faulting, particularly immediately after an earthquake. Thus, the lithosphere may behave more rigidly during the immediate postseismic period than it does averaged over multiple cycles.

5. Conclusions

We attempt to unify the variety of vertical deformation observations surrounding the normal faulting process with one numerical model. The observations can be confusing because shorter-term coseismic and longer-term

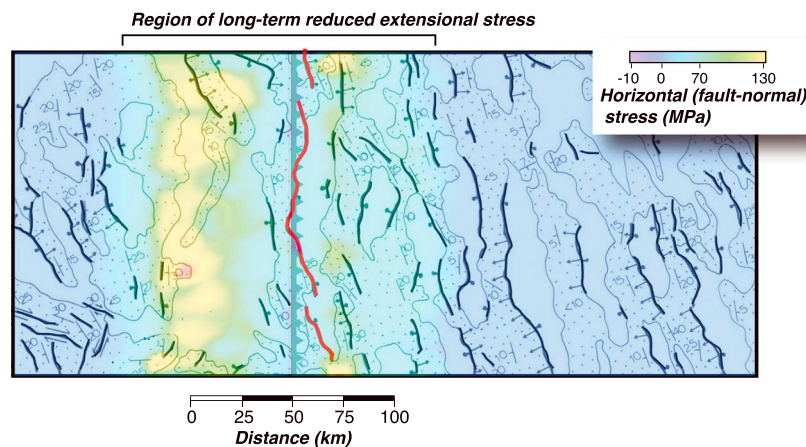


Figure 17. Calculated distribution of horizontal (directed east-west) least principal stress magnitude resulting from long-term slip on a normal fault (red lines) under imposed regional extension. We find a region of persistent least-stress increase that extends ~50–60 km on either side of the fault, where the crust should be resistant to additional normal faulting, and the lower crustal and upper mantle viscosity increased.

postseismic observations are at odds with each other and observed topography. Coseismic deformation occurs as asymmetric fault offset, with nearly all movement expressed as subsidence of the hanging wall. A few decades later, postseismic geodetic data reveal broad, symmetric uplift of both the footwall and hanging wall. The long-term geologic and topographic signature of rifting has sharply bent flanks lifted high above intervening basins.

A simple finite element model can explain these time-dependent features provided it is subject to gravity and has the following components: (1) an elastic upper crustal layer that can undergo permanent deformation (by cracking in our case), (2) a thermally creeping lower crustal layer that is stronger than the upper mantle layer beneath it, and (3) a dipping fault that cuts through the elastic crust and is underlain by an extension through the lower crust that simulates a shear zone or other narrow region of enhanced deformation.

In the model, the following sequence of events occurs in response to applied tectonic extension. 1. Stretching the model from its ends causes the hanging wall to pull away from and then subside along a dipping normal fault (Figure 6). The footwall stays relatively stable during this coseismic period. 2. The model cannot generate stick-slip behavior by itself, so we impose an earthquake with asymmetric slip. Simultaneous unweighting of the footwall and static stress imposed on a lower crustal shear zone beneath the normal fault cause focused uplift of the footwall (Figure 7). During this time (~first 15 years after the earthquake) we see stresses imposed that lead to the sharp (~10 km wavelength) bending of the footwall crest (Figures 9a and 11). 3. By 50–60 years after the earthquake, uplift is less focused but is still mostly concentrated beneath the footwall (Figures 9b and 9c). A relatively strong lower crust causes this to manifest at the surface as a broad upward that affects the hanging wall also (Figure 8), and with lower crustal shearing having exhausted its contribution. 4. Modeling of repeated faulting episodes over millions of years leads to the high-magnitude bending (Figures 12 and 13) of the footwall by isostatic forces. The initially 60° dipping normal fault gradually reduces its dip to lower angles (35°–40°) with high (~10 km) cumulative slip amplitudes (Figure 15).

In summary, the model predicts that the permanent vertical deformation we associate with the long-term topographic signature of rifting occurs shortly (1–2 decades) after each earthquake in a narrow zone under the footwall. The intermediate-term (5–20 decades) postseismic deformation has a much longer wavelength (hundreds of kilometers) and lower amplitude such that it is not so obviously imprinted on the landscape.

A numerical model is necessarily a simplification of the real Earth. We anticipate deviations from our model results in the real world. The fault plane in the model is smooth and straight relative to observed normal faults, and the extension of this fault into the lower crust oversimplifies what is likely a more complex and possibly broader deformation zone. Therefore, we might anticipate a more muted, variable, and possibly delayed postseismic uplift in the footwall and subsidence of the hanging wall than the model predicts. Further, while our simulation of the upper crust as a crackable solid is more realistic than an unbreakable elastic layer, it lacks the ability to form long faults that can concentrate deformation.

Acknowledgments

The authors appreciate the efforts of the Associate Editor and two anonymous reviewers, who provided very helpful and constructive comments/suggestions. Data used are from cited references. Model output in ANSYS format is available upon request from the authors at tparsons@usgs.gov.

References

- Bills, B. G., and G. M. May (1987), Constraints on lithospheric thickness and upper mantle viscosity from isostatic warping of Bonneville, Provo, and Gilbert stage shorelines, *J. Geophys. Res.*, *92*, 11,493–11,508, doi:10.1029/JB092iB11p11493.
- Bills, B. G., K. D. Adams, and S. G. Wesnousky (2007), Viscosity structure of the crust and upper mantle in western Nevada from isostatic rebound patterns of the late Pleistocene Lake Lahontan high shoreline, *J. Geophys. Res.*, *112*, B06405, doi:10.1029/2005JB003941.
- Birch, F. (1966), Compressibility; elastic constants, *Geol. Soc. Am. Mem.*, *97*, 97–173.
- Blackwell, D. D., and M. Richards (2004), Geothermal Map of North America, American Association of Petroleum Geologists, scale 1:6,500,000.
- Brown, L. D. (1987), Lower continental crust: Variations mapped by COCORP deep seismic profiling, *Ann. Geophys.*, *5*, 325–330.
- Brun, J.-P. (1999), Narrow rifts versus wide rifts: Inferences for the mechanics of rifting from laboratory experiments, *Philos. Trans. R. Soc. London, Ser. A*, *357*, 695–712.
- Bryant, W. A., (Comp) (2000), Fault number 67c, Panamint Valley fault zone, southern Panamint Valley section, in Quaternary fault and fold database of the United States: U.S. Geol. Surv. [Available at <http://earthquakes.usgs.gov/hazards/qfaults/>].
- Buck, R. A. (1988), Flexural rotation of normal faults, *Tectonics*, *7*, 959–973, doi:10.1029/TC007i005p0959.
- Bürgmann, R., and G. Dresen (2008), Rheology of the lower crust and upper mantle: Evidence from rock mechanics, geodesy, and field observations, *Annu. Rev. Earth Planet. Sci.*, *36*, 531–567, doi:10.1146/annurev.earth.36.031207.124326.
- Byerlee, J. D. (1978), Friction of rocks, *Pure Appl. Geophys.*, *116*, 615–626.
- Byrd, J. O. D., R. B. Smith, and J. W. Geissman (1994), The Teton fault, Wyoming: Topographic signature, neotectonics, and mechanisms of deformation, *J. Geophys. Res.*, *99*, 20,095–20,122, doi:10.1029/94JB00281.
- Caristan, Y. (1982), The transition from high temperature creep to fracture in Maryland diabase, *J. Geophys. Res.*, *87*, 6781–6790, doi:10.1029/JB087iB08p06781.
- Carter, N. L., and M. C. Tsenn (1987), Flow properties of the lithosphere, *Tectonophysics*, *136*, 27–63, 1987.

- Caskey, S. J., S. G. Wesnousky, P. Zhang, and D. B. Slemmons (1996), Surface faulting of the 1954 Fairview Peak (M_s 7.2) and Dixie Valley (M_s 6.8) earthquakes, Central Nevada, *Bull. Seismol. Soc. Am.*, **86**, 761–787.
- Cassel, E. J., D. O. Breecker, C. D. Henry, T. E. Larson, and D. F. Stockli (2014), Profile of a paleo-orogen: High topography across the present-day Basin and Range from 40 to 23 Ma, *Geology*, **42**, 1007–1010, doi:10.1130/G35924.1.
- Chang, W.-L., R. B. Smith, and C. M. Puskas (2013), Effects of lithospheric viscoelastic relaxation on the contemporary deformation following the 1959 M_w 7.3 Hebgen Lake, Montana, earthquake and other areas of the intermountain seismic belt, *Geochem. Geophys. Geosyst.*, **14**, 1–17, doi:10.1029/2012GC004424.
- Christensen, N. I. (1996), Poisson's ratio and crustal seismology, *J. Geophys. Res.*, **101**, 3139–3156, doi:10.1029/95JB03446.
- Christensen, N. I., and W. D. Mooney (1995), Seismic velocity structure and composition of the continental crust: A global view, *J. Geophys. Res.*, **81**, 3047–3054, doi:10.1029/95JB00259.
- Christiansen, R. L., and E. H. McKee (1978), Late Cenozoic volcanic and tectonic evolution of the great basin and Columbia intermontane regions, *Mem. Geol. Soc. Am.*, **152**, 283–311.
- Colgan, J. P., T. A. Dumitru, P. W. Reiners, J. L. Wooden, and E. L. Miller (2006), A regional synthesis of new and existing geologic and thermochronologic Cenozoic tectonic evolution of the Basin and Range province in northwestern Nevada, *Am. J. Sci.*, **306**, 616–654, doi:10.2475/08.2006.02.
- Colgan, J. P., D. L. Shuster, and P. W. Reiners (2008), Two-phase Neogene extension in the northwestern Basin and Range recorded in a single thermochronology sample, *Geology*, **36**, 631–634, doi:10.1130/G24897A.1.
- Compton, R. R. (1966), Analysis of Pliocene-Pleistocene deformation and stresses in northern Santa Lucia Range, California, *Bull. Geol. Soc. Am.*, **77**, 1361–1380.
- Das, S., and C. Scholz (1981), Off-fault aftershock clusters caused by shear stress increase?, *Bull. Seismol. Soc. Am.*, **71**, 1669–1675.
- DeCelles, P. G. (2004), Late Jurassic to Eocene evolution of the Cordilleran thrust belt and foreland basin system, western U.S., *Am. J. Sci.*, **304**, 105–168, doi:10.2475/ajs.304.2.105.
- Dempsey, D. E., S. M. Ellis, R. A. Archer, and J. V. Rowland (2012), The energetics of normal earthquakes on dip-slip faults, *Geology*, **40**, 275–278, doi:10.1130/G32643.1.
- Deng, J., M. Gurnis, H. Kanamori, and E. Hauksson (1998), Viscoelastic flow in the lower crust after the 1992 Landers California, earthquake, *Science*, **282**, 1689–1692, doi:10.1126/science.282.5394.1689.
- Dickinson, W. R. (2006), Geotectonic evolution of the Great Basin, *Geosphere*, **2**, 353–368, doi:10.1130/GES00054.1.
- Doser, D. I. (1986), Earthquake processes in the Rainbow Mountain-Fairview Peak-Dixie Valley, Nevada region 1954–1959, *J. Geophys. Res.*, **91**, 12,572–12,586, doi:10.1029/JB091iB12p12572.
- Doser, D. I. (1988), Source parameters of earthquakes in the Nevada seismic zone, 1915–1943, *J. Geophys. Res.*, **93**, 15,001–15,015, doi:10.1029/JB093iB12p15001.
- Duffield, W. A., and R. D. Weldin (1976), Mineral resources of the South Warner Wilderness, Modoc County, California, *U.S. Geol. Surv. Bull.*, **B1385**, 31 p.
- Ebinger, C. J., G. D. Karner, and J. K. Weissel (1991), Mechanical strength of extended continental lithosphere: Constraints from the Western rift system, East Africa, *Tectonics*, **10**, 1239–1256, doi:10.1029/91TC00579.
- Egger, A. E., and E. L. Miller (2011), Evolution of the northwestern margin of the Basin and Range: The geology and extensional history of the Warner Range and environs, northeastern California, *Geosphere*, **7**(3), 756–773, doi:10.1130/GES00620.1.
- Ehlers, T. A., S. D. Willett, P. A. Armstrong, and D. S. Chapman (2003), Exhumation of the central Wasatch Mountains, Utah: 2. Thermokinematic model of exhumation, erosion, and thermochronometer interpretation, *J. Geophys. Res.*, **108**(B3), 2173, doi:10.1029/2001JB001723.
- Flesch, L. M., W. E. Holt, A. J. Haines, L. Wen, and B. Shen-Tu (2007), The dynamics of western North America: Stress magnitudes and the relative role of gravitational potential energy, plate interaction at the boundary and basal tractions, *Geophys. J. Int.*, **169**, 866–896, doi:10.1111/j.1365-246X.2007.03274.x.
- Freed, A. M., R. Bürgmann, and T. Herring (2007), Far-reaching transient motions after Mojave earthquakes require broad mantle flow beneath a strong crust, *Geophys. Res. Lett.*, **34**, L19302, doi:10.1029/2007GL030959.
- Friedrich, A. M., J. Lee, B. P. Wernicke, and K. Sieh (2004), Geologic context of geodetic data across a Basin and Range normal fault, Crescent Valley, Nevada, *Tectonics*, **23**, TC2015, doi:10.1029/2003TC001528.
- Gourmelen, N., and F. Amelung (2005), Postseismic mantle relaxation in the Central Nevada seismic belt, *Science*, **310**, 1473–1476, doi:10.1126/science.1119798.
- Hammond, W. C., and W. Thatcher (2004), Contemporary tectonic deformation of the Basin and Range province, western United States: 10 years of observation with the Global Positioning System, *J. Geophys. Res.*, **109**, B08403, doi:10.1029/2003JB002746.
- Hammond, W. C., C. Kreemer, and G. Blewitt (2009), Geodetic constraints on contemporary deformation in the northern Walker Lane: 3. Central Nevada seismic belt postseismic relaxation, *Geol. Soc. Am. Spec. Pap.*, **447**, 33–54.
- Hammond, W. C., G. Blewitt, Z. Li, H.-P. Plag, and C. Kreemer (2012), Contemporary uplift of the Sierra Nevada, western United States, from GPS and InSAR measurements, *Geology*, **40**, 667–670, doi:10.1130/G32968.1.
- Hampel, A., and R. Hetzel (2015), Horizontal surface velocity and strain patterns near thrust and normal faults during the earthquake cycle: The importance of viscoelastic relaxation in the lower crust and implications for interpreting geodetic data, *Tectonics*, **34**, 731–752, doi:10.1002/2014TC003605.
- Hansen, F. D., and N. L. Carter (1983), Semibrittle creep of dry and wet Westerly granite at 1000 MPa, 24th U.S. Symposium on Rock Mechanics, pp. 429–447, Texas A&M Univ., College Station, Tex.
- Harry, D. L., D. S. Sawyer, and W. P. Leeman (1993), The mechanics of continental extension in western North America: Implications for the magmatic and structural evolution of the Great Basin, *Earth Planet. Sci. Lett.*, **117**, 59–71.
- Hassani, R., and J. Chéry (1996), Anelasticity explains topography associated with Basin and Range topography, *Geology*, **24**, 1095–1098.
- Heiskanen, W. A., and F. A. Vening Meinesz (1958), Faulting and graben development as a consequence of uniaxial stress release in the crust, 390–394, in *The Earth and its Gravity Field*, 470 pp., McGraw Hill, New York.
- Hetland, E. A., and B. H. Hager (2003), Postseismic relaxation across the Central Nevada seismic belt, *J. Geophys. Res.*, **108**(B8), 2394, doi:10.1029/2002JB002257.
- Hodgkinson, K. M., R. S. Stein, and G. Marshall (1996), Geometry of the 1954 Fairview Peak-Dixie Valley earthquake sequence from a joint inversion of leveling and triangulation data, *J. Geophys. Res.*, **101**(B11), 25,437–25,457, doi:10.1029/96JB01643.
- Holbrook, W. S., R. D. Catchings, and C. M. Jarchow (1991), Origin of deep crustal reflections: Implications of coincident seismic refraction and reflection data in Nevada, *Geology*, **19**, 175–179.
- Holmes, A. (1965), *Principles of Physical Geology*, Thomas Nelson, London.

- Huisman, R. S., and C. Beaumont (2002), Asymmetric lithospheric extension: The role of frictional plastic strain softening inferred from numerical experiments, *Geology*, **30**, 211–214.
- Jarchow, C. M., G. A. Thompson, R. D. Catchings, and W. D. Mooney (1993), Seismic evidence for active magmatic underplating beneath the Basin and Range province, western United States, *J. Geophys. Res.*, **98**(B12), 22,095–22,108, doi:10.1029/93JB02021.
- Karow, T., and A. Hampel (2010), Slip rate variations on faults in the Basin-and-Range Province caused by regression of Late Pleistocene Lake Bonneville and Lake Lahontan, *Int. J. Earth Sci. (Geol. Rundsch.)*, **99**, 1941–1953, doi:10.1007/s00531-009-0496-3.
- King, G. C. P., R. S. Stein, and J. B. Rundle (1988), The growth of geological structures by repeated earthquakes 1: Conceptual framework, *J. Geophys. Res.*, **93**, 13,307–13,318, doi:10.1029/JB093iB11p13307.
- Kirby, S. H., and A. K. Kronenberg (1987), Rheology of the lithosphere: Selected topics, *Rev. Geophys.*, **25**, 1219–1244, doi:10.1029/RG025i006p01219.
- Klemperer, S. L., T. A. Hauge, E. C. Hauser, J. E. Oliver, and C. J. Potter (1986), The Moho in the northern Basin and Range, Nevada, along the COCORP 40°N seismic-reflection transect, *Geol. Soc. Am. Bull.*, **97**, 603–618.
- Koseluk, R. A., and R. E. Bischke (1981), An elastic rebound model for normal fault earthquakes, *J. Geophys. Res.*, **86**, 1081–1090, doi:10.1029/JB086iB02p01081.
- Lachenbruch, A. H. (1968), Preliminary geothermal model of the Sierra Nevada, *J. Geophys. Res.*, **73**, 6977–6989, doi:10.1029/JB073i022p06977.
- Lavier, L. L., and W. R. Buck (2002), Half graben versus large-offset low-angle normal fault: Importance of keeping cool during normal faulting, *J. Geophys. Res.*, **107**(B6), 2122, doi:10.1029/2001JB000513.
- Lavier, L. L., W. R. Buck, and A. N. B. Poliakov (1999), Self-consistent rolling-hinge model for the evolution of large-offset low-angle normal faults, *Geology*, **27**, 1127–1130.
- Lavier, L. L., W. R. Buck, and A. N. B. Poliakov (2000), Factors controlling normal fault offset in an ideal brittle layer, *J. Geophys. Res.*, **105**, 23,431–23,442, doi:10.1029/2000JB900108.
- Lerch, D. W., S. L. Klemperer, A. E. Egger, J. P. Colgan, and E. L. Miller (2010), The northwestern margin of the Basin-and-Range Province, part 1: Reflection profiling of the moderate-angle (~30°) Surprise Valley Fault, *Tectonophysics*, **488**, 143–149, doi:10.1016/j.tecto.2009.05.028.
- Liu, M. (2001), Cenozoic extension and magmatism in the North American Cordillera: The role of gravitational collapse, *Tectonophysics*, **342**, 407–433.
- Liu, M., and K. P. Furlong (1994), Intrusion and underplating of mafic magmas: Thermal-rheological effects and implications for Tertiary tectonomagmatism in the North American Cordillera, *Tectonophysics*, **237**(175–179), 182–187.
- Liu, M., and Y. Shen (1998), Crustal collapse, mantle upwelling, and Cenozoic extension in the North American Cordillera, *Tectonics*, **17**, 311–321, doi:10.1029/98TC00313.
- Lucchitta, I. (1990), Role of heat and detachment in continental extension as viewed from the eastern Basin and Range province in Arizona, *Tectonophysics*, **174**, 77–114.
- McClaskey, G. C., B. D. Kilgore, D. A. Lockner, and N. M. Beeler (2014), Laboratory generated $M = 6$ earthquakes, *Pure Appl. Geophys.*, **171**, 2601–2615.
- Meissner, R. (1986), *The Continental Crust*, *Int. Geophys. Ser.*, vol. 34, 426 pp., Academic Press, Orlando, Fla.
- Meister, L. J., R. O. Burford, G. A. Thompson, and R. L. Kovach (1968), Surface strain changes and strain energy release in the Dixie Valley-Fairview Peak area, Nevada, *J. Geophys. Res.*, **73**, 5981–5994, doi:10.1029/JB073i018p05981.
- Nishimura, T., and W. Thatcher (2003), Rheology of the lithosphere inferred from postseismic uplift following the 1959 Hebgen Lake earthquake, *J. Geophys. Res.*, **108**(B8), 2389, doi:10.1029/2002JB002191.
- Okada, Y. (1992), Internal deformation due to shear and tensile faults in a half space, *Bull. Seismol. Soc. Am.*, **82**, 1018–1040.
- Parsons, T. (1995), The Basin and Range province, in *Continental Rifts: Evolution, Structure and Tectonics*, edited by K. Olsen, pp. 277–324, Elsevier, Amsterdam.
- Parsons, T. (2002), Global Omori law decay of triggered earthquakes: Large aftershocks outside the classical aftershock zone, *J. Geophys. Res.*, **107**(B9), 2199, doi:10.1029/2001JB000646.
- Pollitz, F. F., G. Peltzer, and R. Bürgmann (2000), Mobility of continental mantle: Evidence from postseismic geodetic observations following the 1992 Landers earthquake, *J. Geophys. Res.*, **105**, 8035–8054, doi:10.1029/1999JB900380.
- Proffett, J. M., Jr. (1977), Cenozoic geology of the Yerington district, Nevada, and implications for the nature and origin of Basin and Range faulting, *Geol. Soc. Am. Bull.*, **88**, 247–266.
- Putirka, K., and B. Platt (2012), Basin and Range volcanism as a passive response to extensional tectonics, *Geosphere*, **8**, 1274–1285, doi:10.1130/GES00803.1.
- Segall, P. (2010), *Earthquake and Volcano Deformation*, 432 pp., Princeton Univ. Press, Princeton, N. J.
- Stein, R. S., and S. E. Barrientos (1985), Planar high-angle faulting in the Basin and Range: Geodetic analysis of the 1983 Borah Peak, Idaho, earthquake, *J. Geophys. Res.*, **90**, 11,355–11,366, doi:10.1029/JB090iB13p11355.
- Stein, R. S., and M. Lisowski (1983), The 1979 Homestead Valley earthquake sequence, California: Control of aftershocks and postseismic deformation, *J. Geophys. Res.*, **88**, 6477–6490, doi:10.1029/JB088iB08p06477.
- Stein, R. S., G. C. P. King, and J. B. Rundle (1988), The growth of geological structures by repeated earthquakes 2: Field examples of continental dip-slip faults, *J. Geophys. Res.*, **93**, 13,319–13,331, doi:10.1029/JB093iB11p13319.
- Stewart, J. H. (1978), 1: Basin-range structure in western North America: A review, *Geol. Soc. Am. Mem.*, **152**, 1–32, doi:10.1130/MEM152-p1.
- Stewart, J. H. (1998), Regional characteristics, tilt domains, and extensional history of the later Cenozoic Basin and Range province, western North America, *Geol. Soc. Am. Spec. Pap.*, **323**, 47–74, doi:10.1130/0-8137-2323-X.47.
- Stewart, J. H., J. E. Carlson, G. L. Raines, K. A. Connors, L. A. Moyer, and R. J. Miller (2003), Spatial digital database for the geologic map of Nevada, *U.S. Geol. Surv. Open File Rep.*, **03-66**, 32 p.
- Stiros, S. C., P. Psimoulis, and S. Pitharoulis (2007), Geodetic constraints to the kinematics of the Kapareli fault, reactivated during the 1981, Gulf of Corinth earthquakes, *Tectonophysics*, **440**, 105–119.
- Stockli, D. F., T. A. Dumitru, M. O. McWilliams, and K. A. Farley (2003), Cenozoic tectonic evolution of the White Mountains, California and Nevada, *Bull. Geol. Soc. Am.*, **115**, 788–816.
- Thompson, G. A., and T. Parsons (2009), Can footwall unloading explain late Cenozoic uplift of the Sierra Nevada crest?, *Int. Geol. Rev.*, **51**, 986–993, doi:10.1080/00206810903059156.
- Upcott, N. M., R. K. Mukasa, C. J. Ebinger, and G. D. Karner (1996), Along-axis segmentation and isostasy in the western rift, East Africa, *J. Geophys. Res.*, **101**, 3247–3268, doi:10.1029/95JB01480.
- Van Buer, N. (2012), Preliminary geologic map of the Sahwawe and Nightingale ranges, Churchill, Pershing, and Washoe Counties, Nevada, Nevada Bureau of Mines and Geology, *Open File Rep.*, **12-2**, 1:62,500, 12 pp.
- Vening Meinesz, F. A. (1950), Les graben africains, resultat de compression ou de tension dans la croûte terrestre?, Institut Royal Colonial Belge, *Bull. des Seances*, **21**, 539–552.

- Vogfjord, K. S., and C. A. Langston (1987), The Meckering earthquake of 14 October 1968: A possible downward propagating rupture, *Bull. Seismol. Soc. Am.*, *77*, 1558–1578.
- Wang, L., R. Wang, F. Roth, B. Enescu, S. Hainzl, and S. Ergintav (2009), Afterslip and viscoelastic relaxation following the 1999 M 7.4 Izmit earthquake from GPS measurements, *Geophys. J. Int.*, *178*, 1220–1237, doi:10.1111/j.1365-246X.2009.04228.x.
- Wannamaker, P. E., et al. (2008), Lithospheric dismemberment and magmatic processes of the Great Basin–Colorado Plateau transition, Utah, implied from magnetotellurics, *Geochim. Geophys. Geosyst.*, *9*, Q05019, doi:10.1029/2007GC001886.
- Watts, A. B., and E. B. Burov (2003), Lithospheric strength and its relationship to the elastic and seismogenic layer thickness, *Earth Planet. Sci. Lett.*, *213*, 113–131.
- Wells, D. L., and K. J. Coppersmith (1994), New empirical relationships among magnitude, rupture length, rupture width, rupture area, and surface displacement, *Bull. Seismol. Soc. Am.*, *84*, 974–1002.
- Wernicke, B. P., A. M. Friedrich, N. A. Niemi, R. A. Bennett, and J. L. Davis (2000), Dynamics of plate boundary fault systems from Basin and Range Geodetic Network (BARGEN) and geologic data, *GSA Today*, *10*(11), 1–7.
- Whitten, C. A. (1957), Geodetic measurements in the Dixie Valley area, *Bull. Seismol. Soc. Am.*, *47*, 321–325.
- Willam, K. J., and E. P. Warnke (1975), Constitutive models for the triaxial behavior of concrete, *Proc. Int. Assoc. Bridge Struct. Eng.*, *19*, 1–30.
- Yamashina, K. (1978), Induced earthquakes in the Izu Peninsula by the Izu-Hanto-Oki earthquake of 1974, Japan, *Tectonophysics*, *51*, 139–154.
- Zeyen, H., F. Volker, V. Wehrle, K. Fuchs, S. V. Sobolev, and R. Altherr (1997), Styles of continental rifting: Crust–mantle detachment and mantle plumes (Review), *Tectonophysics*, *278*, 329–352.